CFD Simulation of Cloud and Tip Vortex Cavitation on Hydrofoils

Th. Frank[1], C. Lifante[1], S. Jebauer[1], M. Kuntz[1] and K. Rieck[2]

[1)] ANSYS Germany, CFX Development
Staudenfeldweg 12, D-83624 Otterfing, Germany
Thomas.Frank@ansys.com , Conxita.Lifante@ansys.com

[2)] Schiffsbau-Versuchsanstalt Potsdam GmbH (SVA)
Marquardter Chaussee 100, D-14469 Potsdam, Germany
Rieck@SVA-Potsdam.de

Keywords: cavitation, CFD, validation

Abstract

The onset of cavitation around propellers, hydrofoils, ships, etc represents an important issue in terms of reduced performance, erosion and passenger/crew comfort due to cavitation induced vibrations and noise among other drawbacks. Consequently cavitation has been studied by many researchers, but up to now most of the investigations are still experiments. Since experimental investigations for marine applications are expensive, CFD simulations represent a powerful tool in order to investigate the phenomenon and consequently to improve the design of such components. A model to deal with cavitation and the pressure fluctuations introduced by it has been developed in ANSYS CFX, and a validation of it has been carried out. Two test cases have been chosen for this purpose. The first one is a 2D case containing a plano-convex profile, where cloud cavitation can be observed. The second one consists of a 3D case, where the fluid flows around a NACA 66_2-415 hydrofoil. A tip vortex is generated with high radial velocity gradients originating cavitation. In both cases the simulations have been carried out on refined grids and the numerical results have been compared to those in literature, showing good agreement with them in most of the cases.

1. Introduction – Cavitation Modelling for Marine Applications

Cavitation in marine applications like flows around hydrofoils, ships and propellers is a phenomenon, which can lead to serious performance deterioration of propellers, to cavitation erosion damages to propeller blades and to the loss of passenger comfort due to cavitation induced pressure fluctuations interacting with the ship hull. Therefore large experimental and simulation efforts are spent into the investigation of cavitation inception and accurate prediction of cavitation for existing and new marine technology designs. Due to high operational costs of experimental investigations in scaled cavitation tunnels and uncertainties in the upscaling from the experimental data to real scale designs it is highly desirable to be able to study cavitation with reliable and accurate CFD simulation techniques.

The aim of the presented work is the further development of a cavitation model in ANSYS CFX and validation against available experimental data. The cavitation model in ANSYS CFX is based on the homogeneous multiphase flow framework of the CFD solver taking into account the dynamics of the cavitation bubbles by solving a simplified Rayleigh-Plesset equation for the cavitation bubble radius. The cavitation model can be combined with any of the turbulence models, which are available in ANSYS CFX, where the SST turbulence model of Menter [6] has been chosen as the basis for the present study. Turbulent pressure fluctuations and their influence on the cavitation process can be taken into account either by resolving them in the numerical simulation, by applying a large scale resolving turbulence model (e.g. LES/DES/SAS) or by relating them to the turbulent kinetic energy and taking into account an additional pressure fluctuation term in the Rayleigh-Plesset equation.

The validation of the ANSYS CFX cavitation model (Jebauer, [4]) was based on available literature data from Le et al. [5], Franc [3] and Arndt & Dugue [2]. In the first test case a plano-convex profile with cavitation clouds on upper and lower side has been studied in a two-dimensional configuration. Cavitation inception, cavitation bubble sizes and hydrofoil lift have been examined for different angles of attack and for different cavitation numbers. Transient averaged pressure profiles on the hydrofoil upper and lower side have been compared against experimental data for different flow regimes.

The second test case was the flow around a NACA 66_2-415 hydrofoil with elliptical planform, where the formation of a tip vortex can be observed. High radial velocity gradients lead to low pressure below saturation pressure in the vortex core inducing cavitation. The expected cavitation inception in the vortex core has been investigated and compared to a correlation vs. lift coefficient and Reynolds number as obtained by Arndt et al. [2] from a large number of experiments. In order to assess the minimum pressure in the trailing vortex core with strong swirling motion and high velocity gradients a curvature correction term in the SST turbulence model was applied, leading to a substantial improvement in the accuracy of predicted fluid velocities. Further enhanced results were obtained by changing the turbulence model to a Reynolds Stress Model [14] [15].

Numerical simulations using ANSYS CFX have been performed on hierarchically refined meshes applying the Best Practice Guidelines by Menter [7]. Comparison of integral data (as hydrofoil lift), transient averaged volume fraction fields and pressure profiles on hydrofoil surface as well as radial velocity profiles in the tip vortex showed good agreement with experimental data. Also for the three-dimensional test case of Arndt & Dugue [2] it was found, that the mesh resolution of the finest mesh was still too coarse in order to fully resolve the very sharp velocity gradients in circumferential fluid velocities in the tip vortex close to the hydrofoil, when using the SST turbulence model.

Nomenclature

r_α Phase volume fraction
u_i Velocity component (m s^{-1})
$\dot{S}_\alpha$ Phase mass transfer rate (Kg m^{-3} s^{-1})
g_i Gravity component (m s^{-2})
P Pressure (N m^{-2})
R_B Bubble radius (m)
$\overline{u}_i$ Average velocity component (m s^{-1})
u_i' Fluctuating velocity component (m s^{-1})
k Kinetic energy (m^2 s^{-2})

Greek letters
ε Turbulence dissipation rate (m^2 s^{-3})
ω Turbulence frequency (s^{-1})
ρ_α Phase density (Kg m^{-3})
τ_{ij} Stress tensor component (Kg m s^{-2})
σ Surface tension coefficient (m^3 s^{-2})

Subsripts
m Mixture
v Vapour
l Liquid
B Bubble
min minimum
sat saturation
in inlet

2. The ANSYS CFX Cavitation Model

The cavitation model developed by ANSYS CFX is based on the Rayleigh-Plesset equation, which describes the growth of a vapour bubble in a liquid. This effect is taken into account by adding a special source term into the continuity equation. A homogeneous approximation to the vapour-water flow is adopted, considering the same velocity field for all phases by assuming that the vapour bubbles are moving with the continuous phase without slip velocity.

The governing equations for the two-phase flow then read:

Continuity equation for each phase

$$\frac{\partial(r_\alpha \rho_\alpha)}{\partial t} + \frac{\partial(r_\alpha \rho_\alpha u_i)}{\partial x_i} = \dot{S}_\alpha \qquad (1)$$

Momentum conservation equation

$$\frac{\partial(\rho_m u_i)}{\partial t} + \frac{\partial(\rho_m u_i u_i)}{\partial x_j} = \frac{\partial P}{\partial x_i} + \rho_m r_\alpha g_i + \frac{\partial(\tau_{ij})}{\partial x_j} \qquad (2)$$

where r_α, u_i, ρ_α, $\dot{S}_\alpha$, g_i, τ_{ij} and P, are the phase volume fraction, the cartesian velocity components, the phase density, the phase mass generation rate, the acceleration components due to gravity, the pressure and the stress tensor, respectively. Subscript *m* refers to mixture properties. Since the sum of all phases must occupy the whole domain volume, the following constraint must be satisfied:

$$\sum_{\alpha=1}^{N} r_\alpha = 1 \qquad (3)$$

where $N = 2$ is the number of phases.
In addition, assuming that the mass sources are due to the interphase mass transfer, it becomes that:

$$\sum_{\alpha=1}^{N} \dot{S}_\alpha = 0 \qquad (4)$$

When only two phases are involved, as occurs with cavitation (vapour and liquid) the mass transfer rates are related by:

$$\dot{S}_v = -\dot{S}_l = \dot{S}_{lv} \,. \qquad (5)$$

The expression to evaluate this source term can be derived from the Rayleigh-Plesset equation, which in its full version can be written as:

$$R_B \frac{d^2 R_B}{dt^2} + \frac{3}{2}\left(\frac{dR_B}{dt^2}\right)^2 + \frac{2\sigma}{R_B} = \frac{P_v - P}{\rho_l}, \qquad (6)$$

where R_B represents the bubble radius, σ is the surface tension coefficient and P_v is the pressure in the bubble, which is assumed to be the vapour pressure. Neglecting the second order terms and the surface tension, the equation reduces to

$$\frac{dR_B}{dt} = \sqrt{\frac{2}{3}\frac{P_v - P}{\rho_l}} \qquad (7)$$

The rate of change of bubble mass is then predicted as:

$$\frac{dm_B}{dt} = \rho_v \frac{dV_B}{dt} = \rho_v 4\pi R_B^2 \sqrt{\frac{2}{3}\frac{P_v - P}{\rho_l}} \qquad (8)$$

Assuming that there are N_B bubbles per unit volume, the vapour volume fraction may be expressed as:

$$r_v = V_B N_B = \frac{4}{3}\pi R_B^3 N_B \qquad (9)$$

And therefore the total interphase mass transfer due to cavitation per unit volume becomes:

$$\dot{S}_{lv} = \frac{3 r_v \rho_v}{R_B}\sqrt{\frac{2}{3}\frac{P_v - P}{\rho_l}} \qquad (10)$$

This expression has been derived assuming bubble growth (evaporation). It can be generalised to include condensation by including an empirical factor (*F*) in the following manner

$$\dot{S}_{lv} = F\,\frac{3 r_v \rho_v}{R_B}\sqrt{\frac{2}{3}\frac{|P_v - P|}{\rho_l}}\,sign(P_v - P) \qquad (11)$$

which may differ for condensation and vaporisation, and it is designed to take into account the fact that both processes occur at different rates, since the condensation process is usually much slower than evaporation.
Despite the fact that the model has been generalised for evaporation and condensation, it requires further modification in the case of evaporation. Evaporation is initiated at nucleation sites. As the vapour volume fraction increases, the nucleation site density must decrease accordingly, since there

is less liquid. For evaporation r_v is replaced by $r_{nuc}(1-r_v)$. The final form of the cavitation model is:

$$\dot{S}_{lv} = \begin{cases} F_{vap}\dfrac{3r_{nuc}(1-r_v)\rho_v}{R_B}\sqrt{\dfrac{2}{3}\dfrac{P_v-P}{\rho_l}} & \text{if } P < P_v \\ F_{cond}\dfrac{3r_v\rho_v}{R_B}\sqrt{\dfrac{2}{3}\dfrac{P_v-P}{\rho_l}} & \text{if } P > P_v \end{cases} \tag{12}$$

And the following model parameters have been applied: $R_B = 10^{-6} m,\ r_{nuc} = 5\times10^{-4},\ F_{vap} = 50,\ F_{cond} = 0.01$.

2.1. Interaction of Cavitation and Turbulence Modelling

Most of the flows that can be observed in nature or engineering processes are turbulent. It is due to the fact that they are three dimensional flows, unsteady and may contain many different length scales, originating a complex process. The Navier-Stokes equations are still valid for turbulent flows. However, turbulent flows span the range of length and time scales involving scales much smaller than the smallest finite volume size. The computing power required for the Direct Numerical Simulation (DNS) of this kind of flows is further beyond the available one, particularly in cases of industrial interest. Major effort has been carried out by the scientific community in order to take into account the turbulent effects on the flow. Different approaches can be applied such as resolving the large-scale turbulent fluctuations containing the major part of the turbulent kinetic energy (LES, DES, SAS) or modelling the phenomena entirely. When attempting to model the turbulence, turbulence viscosity models can be applied. The turbulence or eddy viscosity models are statistical models and consider that the main variables are compound by an average component and an additional time-varying fluctuating one, like

$$u_i = \bar{u}_i + u_i^{'} \tag{13}$$

Introducing this decomposition into the Navier-Stokes equations (1-2) and time-averaging them, the so-called Reynolds Averaged Navier-Stokes (RANS) equations are obtained

$$\frac{\partial(\rho_m\bar{u}_i)}{\partial t} + \frac{\partial(\rho_m\bar{u}_i\bar{u}_i)}{\partial x_j} = \frac{\partial\bar{P}}{\partial x_i} + \rho_m r_\alpha g_i + \frac{\partial}{\partial x_j}(\bar{\tau}_{ij} - \rho_m\overline{u_i^{'}u_j^{'}}) + S_{M_i} \tag{14}$$

Simulation of RANS equations substantially reduces the computational effort in comparison with DNS and it is generally adopted for engineering applications. However, the averaging procedure introduces additional unknown terms containing products of the fluctuating components, which act like additional stresses in the fluid. These stresses are difficult to determine directly and must be modelled by means of additional equations or quantities in order to close the set of equations. Eddy viscosity models assume that the Reynolds stresses can be related to the mean velocity gradients and turbulent viscosity by the gradient diffusion hypothesis in an analogous manner to Newtonian laminar flow as:

$$\rho_m\overline{u_i^{'}u_j^{'}} = \frac{2}{3}\rho_m k\delta_{ij} + \frac{2}{3}\mu_t\frac{\partial}{\partial x_i}\bar{u}_i\delta_{ij} - \mu_t\left(\frac{\partial}{\partial x_j}\bar{u}_i + \frac{\partial}{\partial x_i}\bar{u}_j\right) \tag{15}$$

where μ_t is the eddy viscosity or turbulent viscosity, and needs to be evaluated. In this work a two-equation turbulence model is applied. It represents a good compromise between numerical effort and computational accuracy. Two extra equations must be solved (k-ε, or k-ω), The turbulent viscosity is modelled as the product of a turbulent velocity and turbulent length scale. The turbulent velocity scale is computed from the turbulent kinetic energy (k), and the turbulent length scale is estimated from either the turbulence kinetic dissipation rate (ε) or the turbulence frequency (ω).

A representative of the two-equation models is the SST (Shear Stress Transport) turbulence model. The SST model [6] [19] is based on the combination of two underlying two-equation turbulence models, the industrially wide-spread k-ε -model (Jones and Launder, [22]) , and the k-ω model in the formulation of Wilcox [20][21]. The hybrid procedure consists of the k-equation and a special form of the ω-equation, which enables through changing the value of a blend factor F_1 switching between a ω-equation (F_1=1) and a ε-equation (F_1=0).

The two equations read as:

$$\frac{\partial(\rho_m k)}{\partial t} + \frac{\partial(\rho_m\bar{u}_j k_i)}{\partial x_j} = P_k - \beta^{'}\rho_m k\omega + \frac{\partial}{\partial x_j}\left(\left(\mu + \frac{\mu_t}{\sigma_k}\right)\frac{\partial k}{\partial x_j}\right) \tag{16}$$

and

$$\frac{\partial(\rho_m\omega)}{\partial t} + \frac{\partial(\rho_m\bar{u}_j\omega)}{\partial x_j} = \gamma\frac{1}{\upsilon_t}P_k - \beta\rho_m\omega^2 + \frac{\partial}{\partial x_j}\left(\left(\mu + \frac{\mu_t}{\sigma_k}\right)\frac{\partial\omega}{\partial x_j}\right) + (1-F_1)\rho_m\frac{2\sigma_{\omega 2}}{\omega}\frac{\partial k}{\partial x_j}\frac{\partial\omega}{\partial x_j} \tag{17}$$

The value P_k represents the turbulent kinetic energy production term

$$P_k = \min\left[\mu_t\left(\frac{\partial\bar{u}_i}{\partial x_j} + \frac{\partial\bar{u}_j}{\partial x_i}\right)\frac{\partial\bar{u}_i}{\partial x_j} + \frac{2}{3}\rho_m k\delta_{ij}\frac{\partial\bar{u}_i}{\partial x_j}, 10\bullet\varepsilon\right]$$

while the blending function looks like

$$F_1 = \tanh\left\{\min\left[\max\left(\frac{\sqrt{k}}{\beta^{'}\omega y}, \frac{500\upsilon}{y^2\omega}\right), \frac{4\rho_m\sigma_{\omega 2}k}{CD_{k\omega}y^2}\right]^4\right\},$$

being $CD_{k\omega} = \max\left[2\rho_m\sigma_{\omega 2}\dfrac{1}{\omega}\dfrac{\partial k}{\partial x_i}\dfrac{\partial\omega}{\partial x_i}, 10^{-10}\right]$, $\beta^{'}$=0.0.

Then the turbulent viscosity can be computed as:

$$\mu_t = \rho_m \frac{a_1 k}{\max\left(a_1 \omega s F_2\right)}, \text{ with } s = \sqrt{S_{ij} S_{ji}}, a_1 = 0.31$$

and $F_2 = \tanh\left[\left(\max\left(\frac{2\sqrt{k}}{\beta' \omega y}, \frac{500\upsilon}{y^2 \omega}\right)\right)\right]$.

In order to become free from effects of the curvature or rotation of the overall system, corrections to the model were introduced. One of them was suggested by Spalart and Shur [23], based on the value s/ϖ (ϖ is the thickness of the eddy). A factor introducing a correction of the turbulence sizeis included. For the SST model applied, the correction factor f_r (Langtry and Menter, 2005) for the production term is computed as

$$f_r = \max\left[\min\left(\frac{(1+c_{r1})2r^*}{1+r^*}\left\{1 - c_{r3}\tan^{-1}(c_{r2}\tilde{r})\right\} - c_{r1}, 1.25\right), 0.0\right] \tag{18}$$

where $r^* = \frac{s}{\sqrt{2\tilde{\omega}_{ij}\tilde{\omega}_{ij}}}$; $\tilde{r} = \omega_{ij}^{RC}\left(\frac{2\tilde{\omega}_{ik}}{\tilde{\omega}_G}\right)D^{-1/2}$;

$$\omega_{ij}^{RC} = S_{jk}\left(\frac{DS_{ij}}{Dt} + \left[\varepsilon_{i\min} S_{jn} + \varepsilon_{j\min} S_{in}\right]\Omega_m\right)D^{-1};$$

$$\tilde{\omega}_{ij} = 0.5 \bullet \left[\frac{\partial u_i}{\partial x_j} - \frac{\partial u_j}{\partial x_i}\right] + \varepsilon_{mji}\Omega_m;$$

$$\tilde{\omega}_G = \left(\tilde{\omega}_{12}^2 + \tilde{\omega}_{13}^2 + \tilde{\omega}_{23}^2\right)^{1/2};$$

ε_{mno} is the permutations symbol, Ω_m is the rotation velocity of the system, $D = \max(s^2, c_{r4}, \omega^2)$, c_{r1}=1.0, c_{r2}=2.0, c_{r3}=1.0, c_{r4}=0.09.

When the stress tensor components must be computed more accurately or the underlying assumption of isotropic turbulence is violated, Reynolds Stress Models can be employed. They are based on transport equations for all components of the Reynolds stress tensor and the dissipation rate (or the turbulence frequency). Algebraic Reynolds Stress models solve algebraic equations for each individual component of the tensor, while differential methods solve a differential transport equation. In this case the computational effort is consequently increased. An ω-based Reynolds Stress model was chosen for the present work: the so-called BSL Reynolds stress model. In this case the modelled equations for the Reynolds stresses can be written as follows:

$$\frac{\partial(\rho\tau_{ij})}{\partial t} + \frac{\partial(\overline{u}_k \rho\tau_{ij})}{\partial x_k} = -\rho P_{ij} + \frac{2}{3}\beta' \rho\omega k\delta_{ij} - \rho\Pi_{ij} + \frac{\partial}{\partial x_k}\left(\left(\mu + \frac{\mu_t}{\sigma^*}\right)\frac{\partial \tau_{ij}}{\partial x_k}\right) \tag{19}$$

And the corresponding ω-equation read as:

$$\frac{\partial(\rho\omega)}{\partial t} + \frac{\partial(\overline{u}_k \rho\omega)}{\partial x_k} = \alpha_3 \frac{\omega}{k} P_k - \beta_3 \rho\omega^2 + \frac{\partial}{\partial x_k}\left[\left(\mu + \frac{\mu_t}{\sigma_{\omega 3}}\right)\frac{\partial \omega}{\partial x_k}\right] + (1 - F_1)2\rho\frac{1}{\sigma_2 \omega}\frac{\partial k}{\partial x_k}\frac{\partial \omega}{\partial x_k} \tag{20}$$

Again the model blends from a ω-based model to an ε-based model. In the first case, the following parameters are employed,

$\sigma_1^* = 2.0$, $\sigma_1 = 2.0$, $\beta_1 = 0.075$, $\alpha_1 = 0.553$

while in the second case, they are

$\sigma_2^* = 1.0$, $\sigma_2 = 0.856$, $\beta_2 = 0.0828$, $\alpha_2 = 0.44$.

The blending is done by means of a smooth linear interpolation in a similar way as for the SST method [14].

The constitutive pressure-strain correlation is given by

$$\Pi_{ij} = \beta' C_1 \omega\left(\tau_{ij} + \frac{2}{3}k\delta_{ij}\right) - \hat{\alpha}\left(P_{ij} - \frac{2}{3}P\delta_{ij}\right) - \hat{\beta}\left(D_{ij} - \frac{2}{3}P\delta_{ij}\right) - \hat{\gamma}k\left(S_{ij} - \frac{1}{3}S_{kk}\delta_{ij}\right) \tag{21}$$

where the production tensor P_{ij} is computed as

$$P_{ij} = \tau_{ik}\frac{\partial \overline{u}_j}{\partial x_k} + \tau_{jk}\frac{\partial \overline{u}_i}{\partial x_k}; P = \frac{1}{2}P_{kk} \tag{22}$$

and the tensor D_{ij} as

$$D_{ij} = \tau_{ik}\frac{\partial \overline{u}_k}{\partial x_j} + \tau_{jk}\frac{\partial \overline{u}_k}{\partial x_i} \tag{23}$$

Finally the turbulent viscosity can be computed as

$$\mu_t = \rho\frac{k}{\omega} \tag{24}$$

The values of the coefficients applied by ANSYS CFX for the computation of this model are:

$\beta' = 0.09$, $\hat{\alpha} = (8 + C_2)/11$, $\hat{\beta} = (8C_2 - 2)/11$, $\hat{\gamma} = (60C_2 - 4)/55$, $C_1 = 1.8$, $C_2 = 0.52$

In addition to the turbulence viscosity models, another family of methods can be used known as LES, consisting of filtering the Navier-Stokes equations and the decomposition of the flow variables into a large scale and a small scale. However, this technique is computationally very expensive when it is applied to industrial problems. In this context arises the need of the use of Scale-Adaptive Simulations (SAS). It is an improved URANS formulation, which allows the resolution of the turbulent spectrum in unstable flow conditions. The SAS method [16] is based on the Von Karman length scale. Depending on it, the model adjusts to a URANS simulation, with LES-like behaviour in unsteady regions, or to RANS simulation in stable flow regions.

As it will be shown in next section, it was found that the use of either a scheme or another plays an important role in the simulation. The Reynolds Stress Model applied (BSL RSM) leaded to more accurate predictions of the rotational velocity (which presents a steep profile) in case of tip vortex cavitation than SST computations.

2.2. The Turbulent Pressure Fluctuation Model

As discussed before, the influence of the turbulence on the cavitation process has been widely observed in multiple experimental investigations. A different approach to account for enhancement of cavitation due to turbulent pressure fluctuations consists of relating them to the turbulence kinetic energy. In this case, the threshold pressure has been changed from saturation pressure to

$$P_v = P_{sat} + P_{turb}^{'}, \qquad (25)$$

where

$$P_{turb}^{'} = 0.39\rho k \qquad (26)$$

Thus, the Rayleigh-Plesset equation (10) applied for the computation of the cavitation bubble growth becomes:

$$\frac{dR_B}{dt} = \sqrt{\frac{2}{3}\frac{P_{sat} + P_{turb}^{'} - P}{\rho_l}} \qquad (27)$$

This strategy was found to be not completely physically realistic and therefore a further slight modification was done by the authors in order to make it more rigorous. Since the kinetic energy is related to the turbulence of the liquid phase, water in the current situation, it seemed more appropriate to apply the pressure turbulence term only in its presence. Therefore, the expression (26) was changed to:

$$P_{turb}^{'} = 0.39(1 - r_v)\rho k, \qquad (28)$$

which vanishes when the volume is filled up only with vapour.

3. Model validation

Two different test cases were chosen to validate the ANSYS CFX cavitation model. The first one consists of a two-dimensional test with plano-convex profile, where sheet or cloud cavitation takes place. Main flow characteristics as cavitation inception, cavitation length or hydrofoil lift have been analyzed for different angles of attack and different Reynolds numbers. Results have been compared against experimental data in literature [3][5].
The second validation case studied was a three-dimensional flow around a NACA 66_2-415 hydrofoil with elliptical planform. A tip vortex can be observed with appearing cavitation in its core, due to the high radial velocity gradients and the low pressure (below saturation pressure) at the vortex core location. Cavitation inception at the vortex has been analyzed and compared to correlation vs. lift by Arndt et al [2]. The vortex core shows a strong swirling motion with high velocity gradients. In order to estimate the minimum pressure value at different cross sections behind the tip of the hydrofoil, different turbulence techniques have been applied. Including a curvature correction term in the SST model or employing a Reynolds Stress Model was found to improve significantly the accuracy of predicted fluid velocities. Integral data as lift, transient averaged volume fraction fields or pressure profiles have been compared to those by Arndt [2].
For both test cases the numerical computations were carried out using ANSYS CFX on a hierarchy of three consecutively refined meshes applying the Best Practice Guidelines by Menter [7].

3.1. The Le et al. Test Case – Sheet Cavitation on Plano-Convex Hydrofoil Profile

3.1.1. Test case definition

A schematic of the experimental setup [3] of Le is given in Figure 1. For the original experiment the hydrofoil was at a submersion depth of 20 cm under a free surface. Its upper side is plane and its lower side circular (radius 26 cm) with a maximum thickness of 20mm. The leading edge is rounded with a radius of 1 mm, so that the chord (c_0) is about 196 mm (Figure 1). Experiments involving different angles of attack (from -8° to 8°), different cavitation numbers and different Reynolds numbers (from 10^6 to $2x10^6$, which correspond to inlet velocities from 5 m/s to 10 m/s) were performed as reported in the original publication of Le [3].
The cavitation number (σ) mainly characterising the flow pattern is defined as:

$$\sigma = \frac{P - P_v}{0.5\rho v_{in}^2} \qquad (29)$$

Configurations within the range of values described by Le were chosen to run the numerical computations, and validate the model in ANSYS CFX.

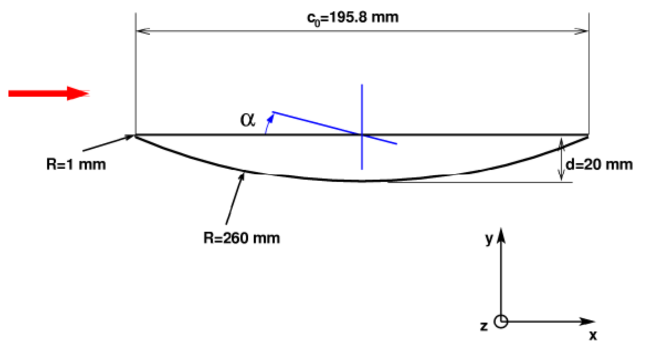

Figure 1: Schematic representation of the flow around a plano-convex hydrofoil.

3.1.2. Mesh hierarchy and CFD setup

The configuration chosen to run the CFD simulations is presented in Figure 2. In difference to the original experimental setup the hydrofoil was submerged in a wall bounded channel, thereby avoiding the prediction of the free surface.

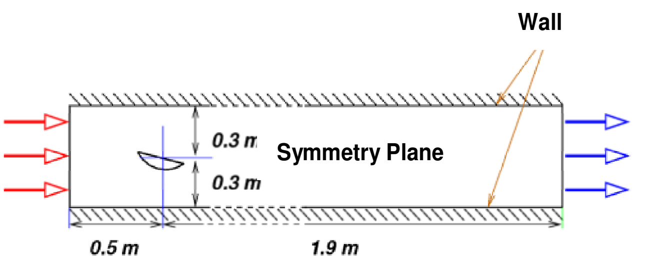

Figure 2: Representation of the setup used for the CFD computations

The discretization of the domain has been performed by using ICEM CFD Hexa as a grid generator. The blocking structure shown in Figure 3 has been designed to generate the grids. In this manner a smooth and high quality mesh can be obtained (in terms of grid lines angle and aspect ratio). In order to apply the Best Practice Guidelines, the simulations were computed on h-refined grids. Three levels of refinement are performed obtaining finer meshes, since the quality of the mesh can determine significantly the accuracy of the simulation executed on it.
The refinement factor is 2 in each coordinate direction, while the minimum grid angle value is around 40° for all three cases. An important attribute of the mesh to take into account is the distance of the first node of the grid to the wall, particularly when turbulence models are applied. For all three meshes this value is small enough to expect a satisfactory resolution of the turbulent boundary layer near the wall. It can be computed as

$$\Delta y = L\sqrt{80}\,\mathrm{Re}_L^{-13/14}\,\Delta y^+ \qquad (30)$$

The grid has been changed not only by refinement but also by rotating the angle of attack of the flow against the hydrofoil in order to deal with different configurations. In this case, the same blocking structure can be employed, and by rotating the blocks adjacent to the hydrofoil, the grids can be updated to the current angle.

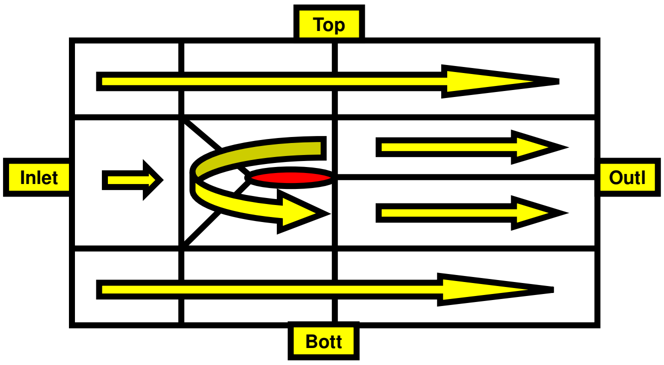

Figure 3: Blocking structure

The main characteristics of the grids created for the numerical simulations are summarized in Table 1, and a representation of one of the coarse meshes involved in the calculations is shown in Figure 4.

Grid	Coarse	Medium	Fine
# nodes	56,452	224,264	893,986
# elements	27,840	111,360	445,440
Minimum grid angle	41	38	43
First layer distance y [µm]	10	5	2.5
Average y^+	4	2	1

Table 1: Grid characteristics

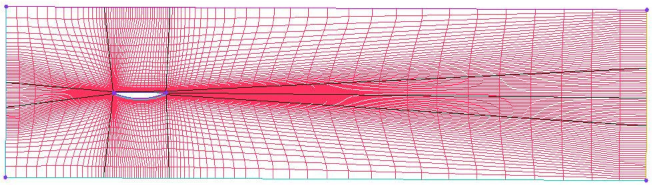

Figure 4: Coarse mesh

Once the meshes were generated, steady state simulations were carried out. However, some configurations appeared to be transient, specifically those with lower cavitation number or larger angle of attack. In these cases the cavitation bubbles become oscillatory or are even partially removed from the hydrofoil surface by the incident fluid flow. Thus, transient simulations had to be carried out for these configurations. The ANSYS CFX setup then must be updated introducing an arithmetical averaging procedure to be applied to the main flow variables, which originates an average pressure, average velocity and average volume fraction field to be compared to the experimental data. The described oscillatory flow behavior can be observed in Figure 5, where a whole transient cycle is shown for a configuration of α=4°, and σ=0.5.

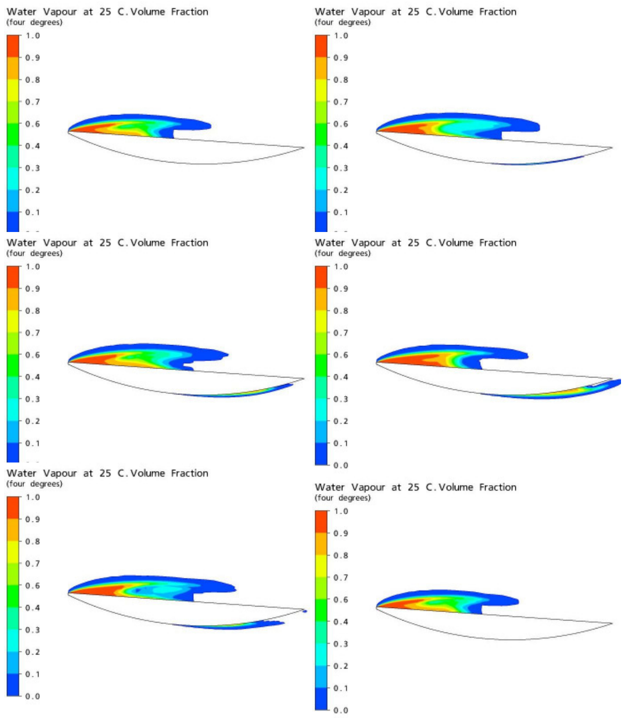

Figure 5; Transient cycle of an oscillating cavitation region on upper side of the hydrofoil for α=4°, and σ=0.5.

3.1.3. Cavitation cavity length

In order to examine cavitation for the different configurations the length of the cavitation zone attached to the upper side of the hydrofoil is measured. An investigation of the influence of both the cavitation number and the angle of attack was performed. It is observed in Figure 6 that the larger the cavitation number is, the lower cavitation length is obtained. In addition, the impact of the angle of attack can be seen. The larger the angle of attack is, the larger becomes the cavitation zone and its length.

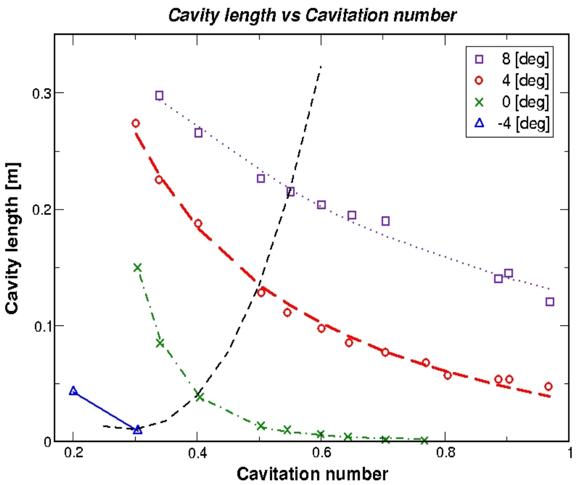

Figure 6: Cavitation length *vs.* cavitation number for different angles of attack

Two representative results of the computed series out of test case conditions are shown in Figure 7 and Figure 8, corresponding to the vapour volume fraction for an angle of attack of α=0° at a cavitation number of σ=0.4 and α=4° with σ=0.5, respectively. For the first case, small cavitating areas appear on both upper and lower side, while for the second case only one larger cavitation bubble appears to be attached to the upper side of the hydrofoil.

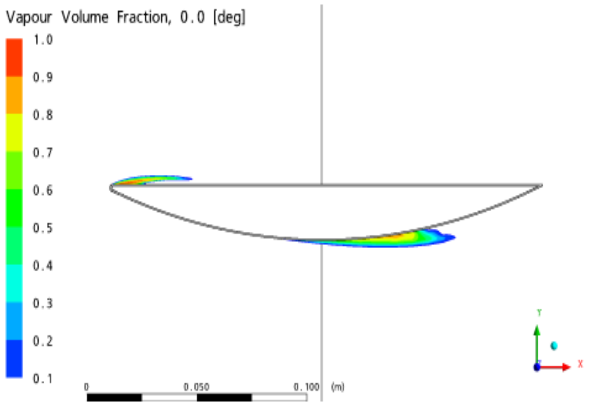

Figure 7: Vapor volume fraction. α=0°, σ=0.4.

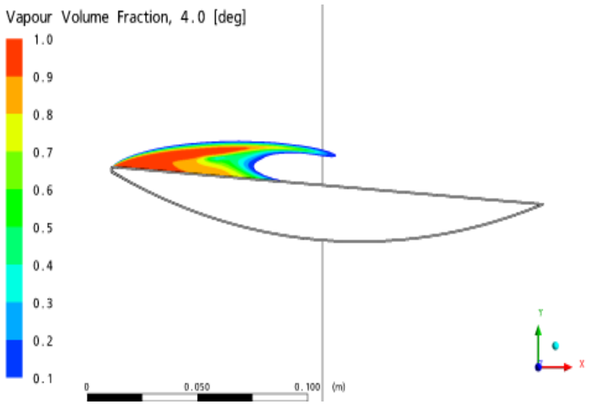

Figure 8: Vapor volume fraction. α=0.4°, σ=0.5.

3.1.4. Pressure coefficient data

The cavitation arises when the pressure drops below the saturation pressure. This can be detected not only by the vapour volume fraction field but also by analyzing the pressure values and comparing to direct pressure measurements at specific locations on the hydrofoil surface. A pressure coefficient can be defined as

$$c_p = \frac{2 \cdot p_{stat}}{\rho_l u_\infty^2} \qquad (31)$$

In Figure 9 to Figure 12**,** the pressure coefficient obtained with medium grid simulations is plotted against the experimental results. They correspond to different angles of attack (α=2.5°, 3.5°, 4.1° and 5.1° respectively), while the cavitation number is 0.55 for the first two cases and 0.81 for Figures 11 and 12. At the zone where the pressure coefficient is lower than the cavitation number, evaporation is occurring. It can be noticed by comparing Figure 9 and Figure 10 that the length of the vapour bubble attached to the upper side of the hydrofoil is larger for the case of α=3.5° as expected. The same effect can be seen in Figure 11 and Figure 12. Nevertheless both predicted cavitation bubble lengths are shorter since the cavitation number is larger. Comparing the different curves to the experimental values reasonable agreement in shape is observed, specifically for the first three configurations while for the larger angle of attack at α=5.1° discrepancies appear.

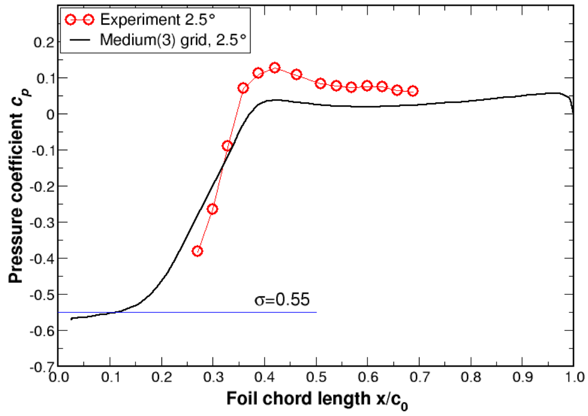

Figure 9: Pressure coefficient, α=2.5°, σ=0.55

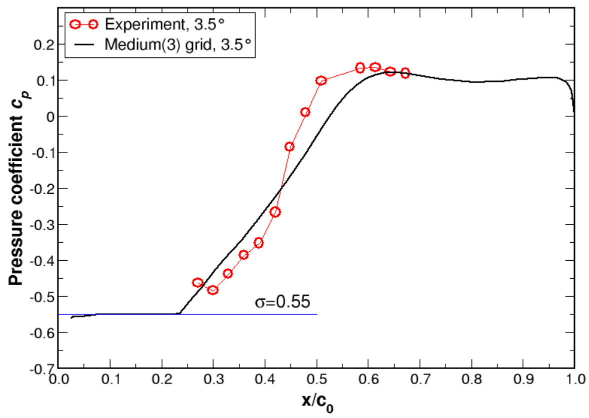

Figure 10: Pressure coefficient, α=3.5°, σ=0.55

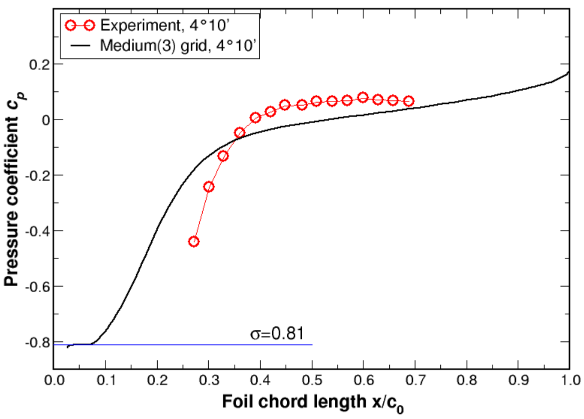

Figure 11: Pressure coefficient, α=4.1°, σ=0.81

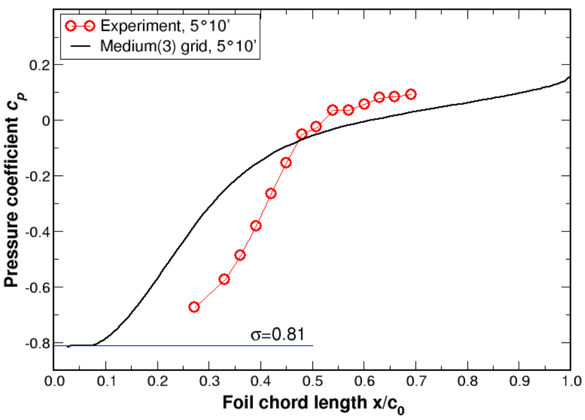

Figure 12: Pressure coefficient, α=5.1°, σ=0.81

Pressure coefficient can be further used to evaluate the influence of turbulent pressure fluctuations on cavitation in accordance with equation (27) and (28). In Figure 13 the c_p curves for three different modelling approaches can be compared. The diagram shows results from a simulation using the original Rayleigh Plesset equation, a simulation using the modification to the Rayleigh-Plesset equation described in equation (26), and finally a simulation using the modification to the Rayleigh-Plesset equation described in equation (28). As mentioned in section 2.2, the last expression leads to more realistic results, also observable differences are not very pronounced for this particular test case.

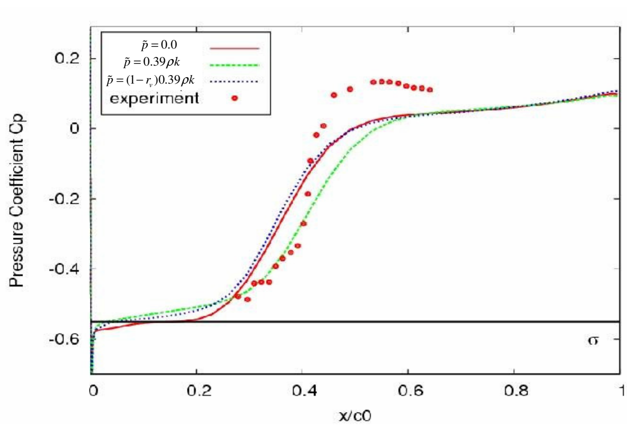

Figure 13; Pressure coefficient in dependency on the modeling approach for the turbulent pressure fluctuation term. α=3.5°, σ=0.55

3.1.5. Lift coefficient

Global values for the different configurations were also investigated and compared to data. This is the case for the lift coefficient, defined as:

$$c_L = \frac{2 \cdot F_L}{\rho_l \cdot u_\infty^2 \cdot A_{blade}} \tag{32}$$

where F_L is the lift force, A_{blade} is the area of the hydrofoil and u_∞ is the velocity far downstream the hydrofoil. Figure 14 shows the value of the lift coefficient for different angles of attack as well as for different cavitation numbers. Under non-cavitating conditions the relationship between lift and angle of attack is almost linear, however this behavior is dramatically modified when the cavitation number is decreased and cavitation appears.

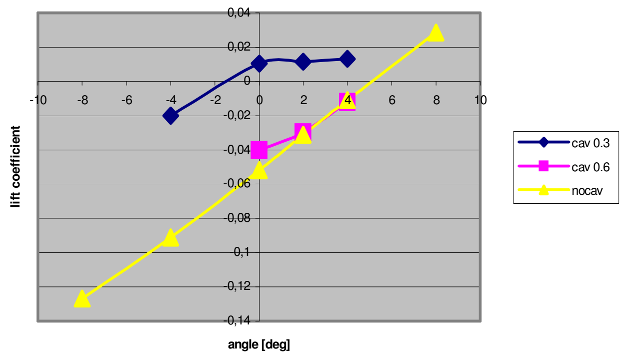

Figure 14: Lift coefficient *vs.* angle of attack for different cavitation number.

3.2. The Arndt et al. Test Case – Tip Vortex Induced Cavitation

3.2.1. Testcase definition

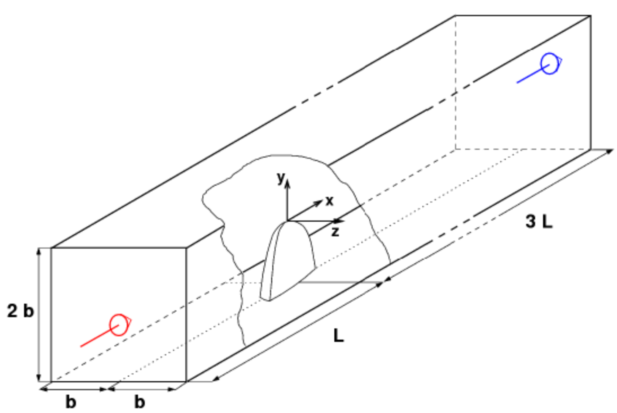

Figure 15: Schematic representation of the NACA 66_2-415 cavitation channel setup

In addition to the plano-convex cavitation test, a three dimensional case consisting of a flow around a NACA 66_2-415 hydrofoil with elliptical planform was investigated. In this case tip-vortex cavitation takes place due to the high radial velocity gradients in the vortex tube, which is released from the tip of the hydrofoil. Highly swirling flow generates

pressure drop below saturation pressure leading to cavitation on the tip of the hydrofoil and in the vortex core of the tip-vortex.
The test body used in the original facility [2][8] consists of an elliptical planform hydrofoil with a chord length of 81mm, a semispan of 95mm and a mean line of 0.8.
Figure 15 shows the representation of the experimental flow geometry which was exactly used for the CFD simulations as well, while in Figure 16 and Figure 17 the details of the planform geometry of the hydrofoil are pointed out.

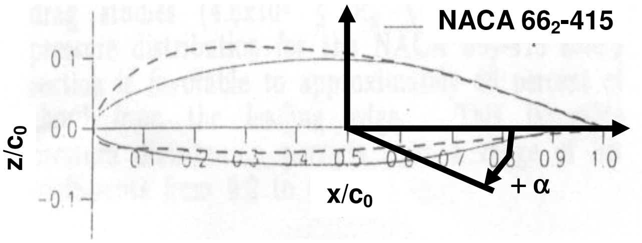

Figure 16: Elliptical profile of the NACA 66_2-415

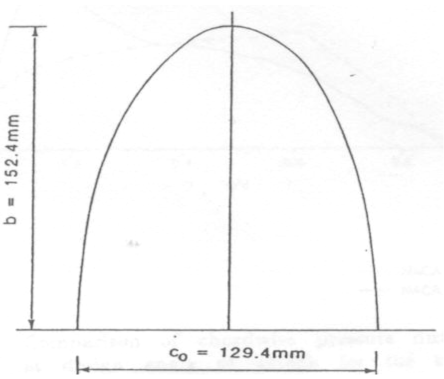

Figure 17: Elliptical profile of the NACA 66_2-415

As for the previous case different configurations were analyzed by changing the angle of attack, the Reynolds number characterising the flow and applying different turbulence modelling approaches (SST, SST with curvature correction term, BSL RSM).
In accordance with the original publication of Arndt an effective angle of attack has been defined as $\alpha_{eff} = \alpha - \alpha_0$, where α_0 corresponds to the zero lift angle, which after a parametric study was chosen as α_0=2.5°.

3.2.2. Mesh hierarchy and CFD setup

The ICEM CFD Hexa grid generator has been used to discretize the domain. A block structure allowing to refine the grid near the blade surface as well as to perform a smooth transition between coarsely resolved areas in the far field and finely resolved areas around the hydrofoil was designed.

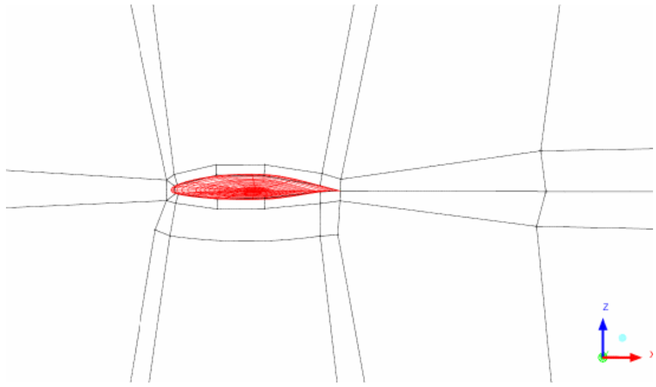

Figure 18: Blocking structure around the hydrofoil

The resulting blocking structure applied near the hydrofoil is shown in Figure 18, while the coarser mesh obtained with this block structure is presented in Figure 19. The designed grid block structure guarantees a minimum grid angle larger then 20° independent from the grid refinement level. As for the previous case an h-refinement study has been carried out, employing three different grids, which are refined by a factor of $\sqrt[3]{4}$ in each coordinate direction. The same parameters were taken into account to evaluate the quality of the mesh: minimum angle formed by the grid lines, aspect ratios and the near wall distance of the first mesh element (computed as in equation (30)). The main information related to the grid properties and grid quality on various mesh levels of refinement used to run the CFD simulations is summarized in Table 2.

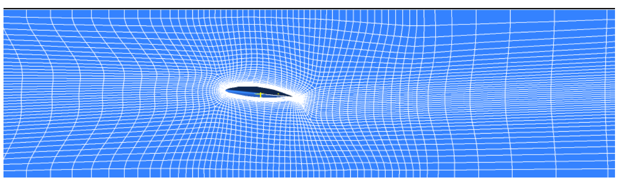

Figure 19: Representation of the meshes employed
.

Grid	Coarse	Medium	Fine
# nodes	358.519	1.394.862	5.442.459
# elements	341.596	1.352.603	5.337.217
Minimum grid angle	20.9	20.7	20.1
First layer distance y [μm]	30	15	7.5
Average y^+	14.3	7.1	3.6

Table 2: Grid characteristics

3.2.3. Tip vortex trajectory

First the shape of the tip vortex trajectory has been investigated. It could be shown that the trajectory does not strongly depend either on the angle of attack, the Reynolds number value or the cavitation number. This effect can be observed in Figure 20, where the tip vortex trajectory obtained for an angle of attack equal to 8.1° and Reynolds number of $9.2x10^5$ is plotted as well as for the case of α=11.6° and $Re=5.2x10^5$ against the experimental values of Arndt.

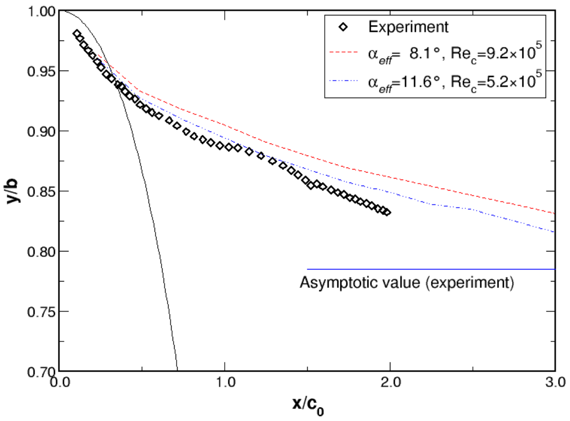

Figure 20: Tip vortex trajectories in the x-y coordinate plane

3.2.4. Resolution of circumferential velocities in the tip vortex

In order to evaluate the quality of the obtained numerical results, the radial velocity profile at different locations has been evaluated. These positions are located near the tip of the hydrofoil and a steep velocity gradient can be observed. Further downstream dissipation of the tip vortex, a reduction in circumferential velocity amplitude as well as in velocity gradient can be observed as the position is departing from the tip. It can be clearly observed in Figure 21, where the velocity profile at the position laying half chord length behind the hydrofoil tip is substantially steeper than the profiles located at a chord length distance or twice chord length distance.

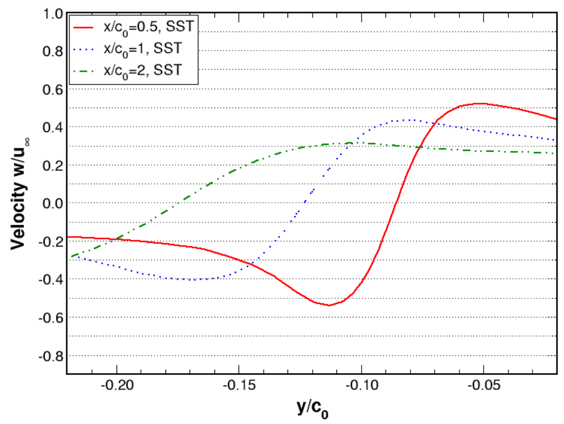

Figure 21: Radial velocity profile at three different locations after the tip vortex for x/c_o=0.5, 1 and 2.

The grid refinement allows to analyze the spatial discretization error of the numerical method and to evaluate if an asymptotical solution independent of the grid resolution can be finally obtained. For this purpose, the radial velocity profile was evaluated using the three refined grids in different locations (Figure 21 and Figure 22). Small differences between the results can be observed even on the highest level of mesh refinement, indicating that a mesh independent solution could not yet be obtained. However, even more severe discrepancies to the experimental results arose, especially on measurement cross section further downstream the hydrofoil where the meshes are coarsening due to axial expansion. While the strong velocity gradients can be predicted for the cross section close to the hydrofoil at x/c_o=0.016, the plotted velocity profiles are much smoother then the experimental data obtained from the experimental facility for x/c_o=1.0 (see Figure 23).

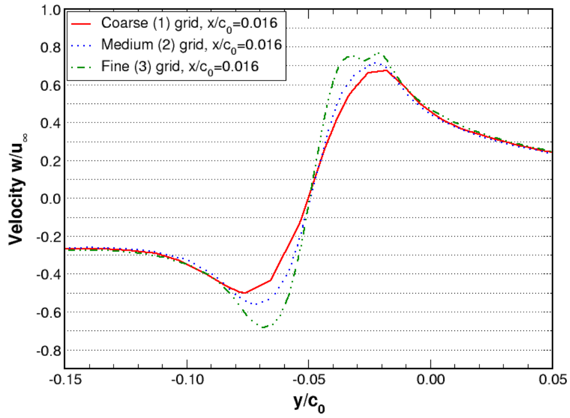

Figure 22: Radial velocity profiles for different grids close to the tip of the hydrofoil.

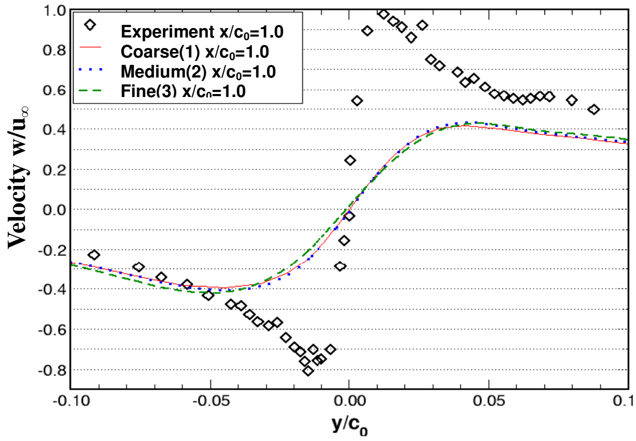

Figure 23: Radial velocity profiles for different grids at a chord length distance from the tip.

A reason for this behaviour is the strong swirl of the velocity field near the tip of the hydrofoil. In order to deal with this effect, different strategies have been considered. The first one consisted of the use of a High Resolution Scheme to solve the turbulence equations, which are solved by default using an upwind advection scheme, which is of cause more diffusive. But the influence of the chosen advection scheme, shown in Figure 24, was found to be not significant. In a second step a curvature correction term in the SST turbulence model had been applied (see section 2.1), in order to account for the strong curvature of streamlines in the tip-vortex flow. The velocity profiles obtained with this curvature correction is also compared in Figure 24, showing an important improvement to approximate the strong velocity gradient.

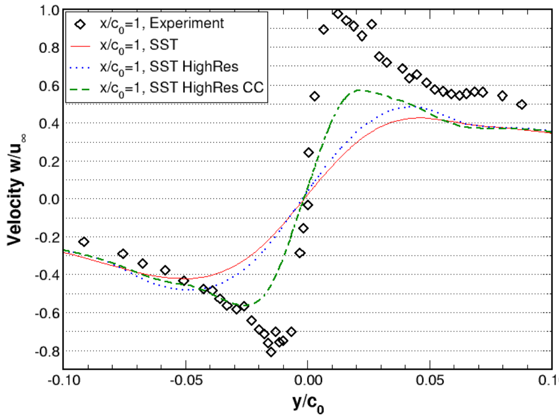

Figure 24: Radial velocity profile with different numerical schemes for solving/modeling the fluid flow turbulence.

A further step was done in order to enhance the evaluation of the velocity gradient near the tip vortex by raising the limitation of assumed isotropic turbulence, which might be not satisfied in the strong swirling flow of the tip vortex behind the hydrofoil. Therefore the turbulence model was changed from a two-equation model (section 2.1) to the BSL Reynolds Stress Model (section 2.1), where not two turbulence model equations but one equation for each Reynolds tensor component is solved. In this case, the computer and memory resources required has been increased, but analyzing Figure 25, it can be noticed that even for coarser meshes the enhancement is significant approaching in a more satisfactory comparison of the steep velocity profile to measurement data.

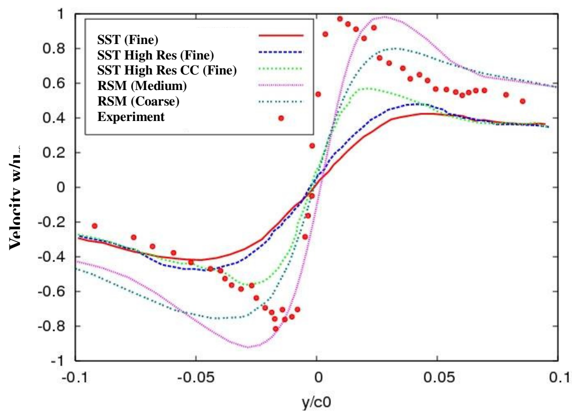

Figure 25: Radial velocity profile for different turbulence modelling

The influence of the turbulence model can also be observed by looking into the vapour volume fraction obtained in an ANSYS CFX multiphase flow simulation applying the cavitation model in combination with SST and BSL RSM turbulence models. A larger tip vortex cavitation zone appears when the BSL Reynolds Stress Model is applied. Sheet cavitation is covering the most of the blade surface for both configurations (Figure 26)

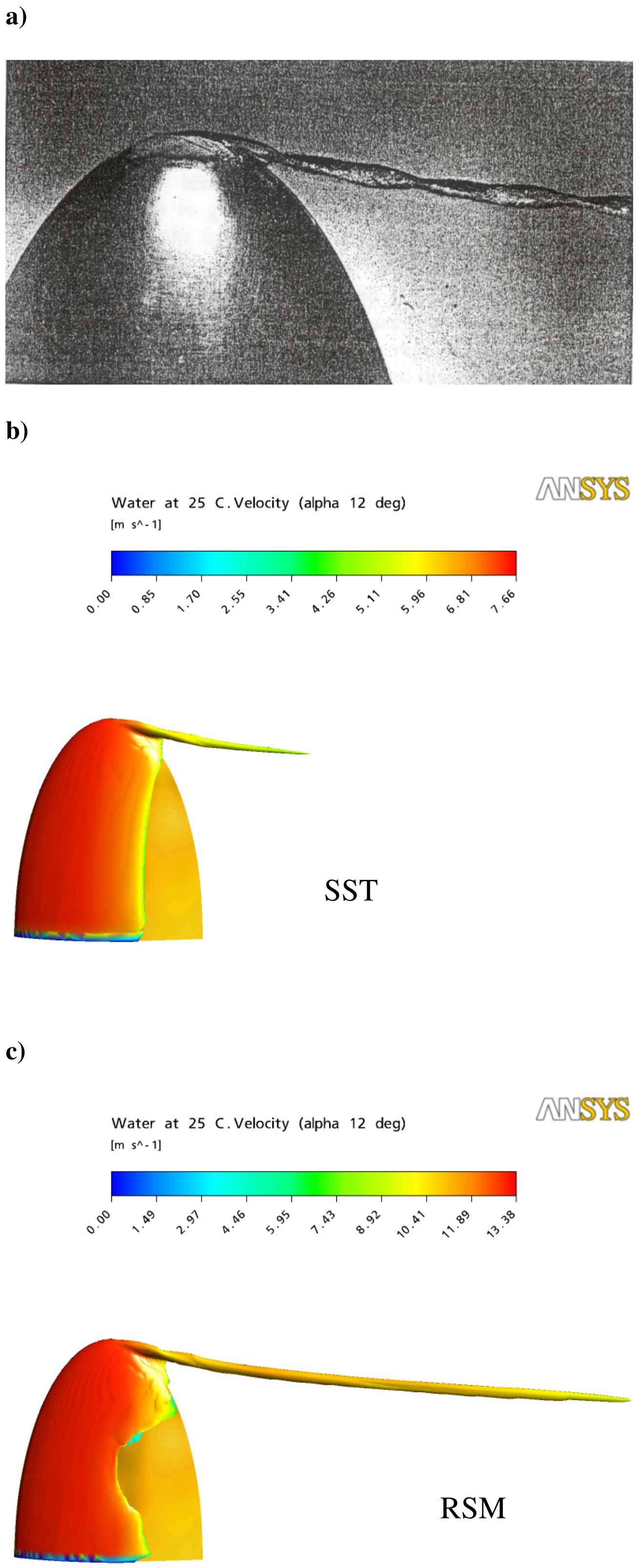

Figure 26: Vapour volume fraction in cavitating flow near the tip. Re=5.2x10^5. σ=0.58.. (a) experimental observation α_{eff}=9.5°, (b) SST turbulence model α_{eff}=12°. (c) BSL Reynolds Stress Model α_{eff}=12°

3.2.5. Lift coefficient

In addition to the tip vortex trajectory and the velocity profiles the value of the lift coefficient (Equation 32) has been investigated.
Figure 27 shows the influence of the angle of attack on the lift coefficient. It has been computed for different Reynolds numbers and by using different grids, however all the computational results are finally arranging between the two experimental results at Obernach [17] and SAFL [8].

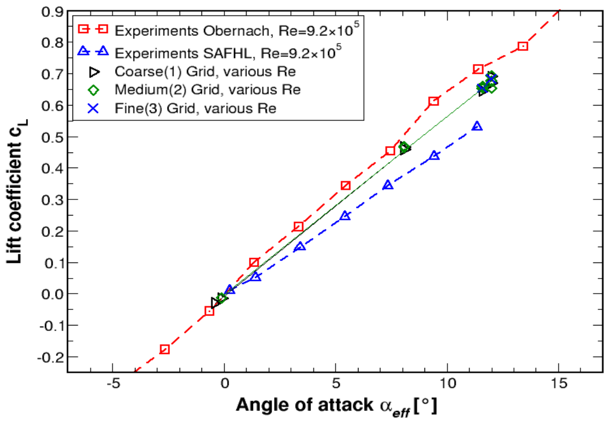

Figure 27: Lift coefficient *vs* angle of attack

The relationship between the cavitation inception, the Reynolds number and the lift coefficient has been considered as well. A correlation can be found in literature for the dependency of these three parameters, which is

$$\sigma_i = 0.063\, c_l^2\ \mathrm{Re}^{0.4} \qquad (33)$$

Results obtained with the three refined grids are compared to the experimental ones, and regressions of the numerical solutions obtained are computed (to compare its slope to the one in equation 33). Figure 28 shows that the slope of the regression curves obtained are lower than the experimental results for the coarse grid, while it increases for the medium grid results. Finally the only result which could be obtained on the finest grid level due to the involved high computational effort is in very good agreement to the experimental results.

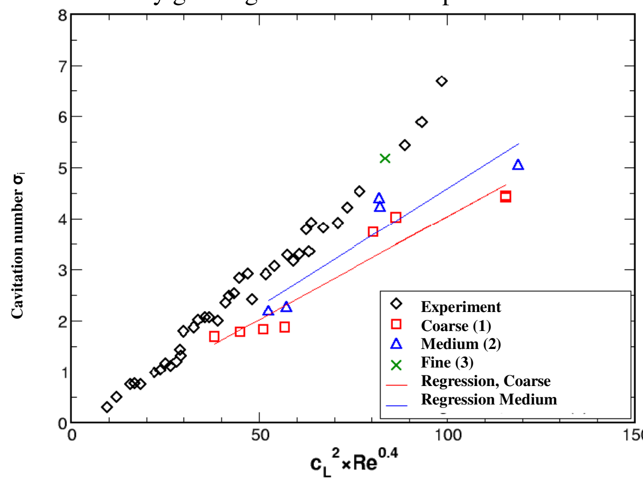

Figure 28: Cavitation inception *vs.* lift coefficient.

Conclusions

A cavitation model in ANSYS CFX has been developed. It is based on a homogeneous multiphase flow approach and on modelling of the bubble dynamics solving the Rayleigh-Plesset equation for cavitation bubble radius. The model has been combined with different turbulence models for the continuous fluid phase. Turbulent pressure fluctuations and their influence on the cavitation phenomena were taken into account by relating them to the turbulent kinetic energy of the continuous phase.
A validation of the model has been performed analyzing two different test cases available from literature and comparing results of the CFD simulations obtained with ANSYS CFX to experimental data.
The first test case is based on the experiments made by [3]. In this test case the flow passes around a plano-convex hydrofoil, and cavitation clouds on both sides can be observed. Three refined grids have been used for the simulation, ensuring comparable mesh quality on all grid levels. The cavitation lengths, pressure coefficients and lift values have been investigated and compared against the literature values. The numerical results agree reasonably well to the experiments, even the necessity to use even finer grids could be shown from the present validation study.
The second test case is based on the experiments by Arndt [2]. Special attention has been paid to the tip vortex, since this is the zone of the flow where larger velocity gradients appear as well as larger pressure drop occur, originating the inception of the tip-vortex cavitation. The trajectory of the tip vortex and the resolution of the radial velocities in the tip vortex have been investigated and compared to data. The velocity gradients were found to be difficult to compute and different strategies have been investigated. The basic simulations were run applying the standard SST turbulence model without any modifications, and it has been observed that the use of high order resolution schemes and the use of a curvature correction term improved the resolution of the steep velocity gradient near the tip of the hydrofoil. In addition, a Reynolds Stress Model has been applied showing a more satisfactory agreement to the numerical results even on coarser grids by taking into account the unisotropy of the continuous phase turbulence in the strong swirling flow in the tip vortex behind the tip of the hydrofoil..

Acknowledgements

Presented investigations have been supported by the German Ministry of Education and Research (BMBF) under grant number 03SX202A.

References

[1] ANSYS Inc., ANSYS CFX 11.0 “Users Manual” (2006).

[2] Arndt, R.E.A., Dugue, C., “Recent Advances in Tip Vortex Cavitation Research”, Proc.The International Symposium on Propulsors and Cavitation, Hamburg, Deutschland, 22.-25. Juni, 1992.

[3] Franc J.P., “Partial Cavity Instabilities and Re-Entrant Jet”,

Keynote Lecture 002, Proc. 4th International Symposium on Cavitation, Pasadena, Kalifornien, U.S.A., 20.-23. June 2001.

[4] Jebauer S., "Numerische Simulation kavitierender Strömungen", Diploma Thesis, TU Dresden, pp. 1-79 (2006).

[5] Le Q., Franc J.P. und Michel J.M., Partial Cavities: "Global Behavior and Mean Pressure Distribution", Journal of Fluids Engineering, Vol. 115-2, S. 243-249 .1993.

[6] Menter F., "Two-Equation Eddy-Viscosity Turbulence Models for Engineering Applications", AIAA Journal, Vol. 32, No. 8, pp. 1598-1605 (1994).

[7] Menter F., "CFD Best Practice Guidelines for CFD Code Validation for Reactor Safety Applications", ECORA Project, pp. 1-47 (2002).

[8] Arndt, R.E.A. and Arakeri, V.H., Higuchi, H., 1991, "Some observations of tip-vortex cavitation", J. Fluid Mechanics, Vol. 229, pp. 269-289

[9] Maines, B.H. and Arndt, R.E.A., 1997, "Tip Vortex Formation and Cavitation", J. Fluids Eng., Vol. 119-2, pp. 413-419

[10] Abbot, I.H. and Doenhoff, A.E. von, 1959, "Theory of Wing Sections", Dover

[11] Maines, B.H., 1995, "Tip Vortex Formation and Cavitation", Dissertation, University of Minnesota, U.S.A.

[12] B., Takacs, T., Willemsen, S., 2001, "CFD Best Practice Guidelines for CFD Code Validation for Reactor-Safety Applications", European Commision, ECORA

[13] Casey, M., Wintergerste, T., 2000, "Best Practice Guidelines, ERCOFTAC Special Interest Group on Quality and Trust in Industrial CFD", Fluid Dynamics Laboratory Sulzer Innotec, 94 p.

[14] Wilcox, D.C., "Multiscale model for turbulent flows", In AIAA 24th Aerospace Sciences Meeting. American Institute of Aeronautics and Astronautics, 1986.

[15] Menter, F.R., "Multiscale model for turbulent flows", In 24th Fluid Dynamics Conference. American Institute of Aeronautics and Astronautics, 1993.

[16] Menter, F.R., and Egorov, Y. "A Scale-Adaptive Simulation Model using Two-Equation Models", AIAA paper 2005-1095, Reno/NV, 2005.

[17] Kjedsen, M. Arndt, R.E.A., Effertzt, M. "Spectral Characteristics of Sheet/Cloud Cavitation". Journal of Fluids Engineering. Vol 122. 2000. pp 481-487

[18] Menter, F., Hemstrom, B., Henriksson, M., Karlsson, R., Latrobe, A., Martin, A., Muhlbauer, P., Scheuerer, M., Smith, B., Takacs, T., Willemsen, S., 2001, "CFD Best Practice Guidelines for CFD Code Validation for Reactor-Safety Applications", European Comission. ECORA,

[19] Menter, F.R., Rumsey, C.L., "Assesment of Two-Equation Turbulence Models for Transonic Flows", AIAA 94-2343, Proc. 25th Fluid Dynamics Conference, Colorado Springs, Colorado, U.S.A., 20.-23. Juni 1994

[20] Wilcox, D.C., 1988, "Reassesment of the Scale-Determining Equation for Advanced Turbulence Models", AIAA J., Vol. 26, S. 1299-1310

[21] Wilcox, D.C., 2000, "Turbulence Modelling for CFD", DCW Industries

[22] Jones, W. P.; Launder, B. E. The Calculation of Low-Reynolds- Number Phenomena with a Two-Equation Model of Turbulence. International Journal for Heat and Mass Transfer 1973,16, 1119 .

[23] Spalart, P.R., Shur, M.L., 1997, „On the sensitization of turbulence models to rotation and curvature", Aerospace Science and Technology, Vol. 1-5, S. 297-302